

Controlled-Controlled-Phase Gates for Superconducting Qubits Mediated by a Shared Tunable Coupler


Niklas J. Glaser^{1,2,*}, Federico Roy^{2,3} and Stefan Filipp^{1,2,4,†}

¹*Physik-Department, Technische Universität München, Garching 85748, Germany*

²*Walther-Meißner-Institut, Bayerische Akademie der Wissenschaften, Garching 85748, Germany*

³*Theoretical Physics, Saarland University, Saarbrücken 66123, Germany*

⁴*Munich Center for Quantum Science and Technology (MCQST), Schellingstraße 4, München 80799, Germany*

 (Received 28 June 2022; revised 21 October 2022; accepted 13 February 2023; published 3 April 2023)

Applications for noisy intermediate-scale quantum computing devices rely on the efficient entanglement of many qubits to reach a potential quantum advantage. Although entanglement is typically generated using two-qubit gates, direct control of strong multiqubit interactions can improve the efficiency of the process. Here, we investigate a system of three superconducting transmon-type qubits coupled via a single flux-tunable coupler. Tuning the frequency of the coupler by adiabatic flux pulses enables us to control the conditional energy shifts between the qubits and directly realize multiqubit interactions. To accurately adjust the resulting controlled relative phases, we describe a gate protocol involving refocusing pulses and adjustable interaction times. This enables the implementation of the full family of pairwise controlled-phase and controlled-controlled-phase gates. Numerical simulations result in fidelities around 99% and gate times below 300 ns using currently achievable system parameters and decoherence rates.

DOI: [10.1103/PhysRevApplied.19.044001](https://doi.org/10.1103/PhysRevApplied.19.044001)

I. INTRODUCTION

Superconducting quantum circuits with fast and high-fidelity single- and two-qubit operations are considered promising candidates for quantum applications [1]. Recent experiments on quantum processors with dozens of superconducting qubits demonstrate the maturity of this platform [2–5] and move this technology well into the era of noisy intermediate-scale quantum (NISQ) devices [6]. Promising NISQ algorithms, such as the variational quantum eigensolver [7–11] for quantum chemistry simulation and the quantum approximate optimization algorithm [12–15] for complex optimization tasks, provide useful applications that do not require error correction. However, these rely on the efficient entanglement of many qubits to ensure that the coherence properties of the quantum system survive over the runtime of the algorithm.

The standard approach for generating multiqubit entanglement is the digital decomposition of multiqubit operations into a discrete set of native single- and two-qubit

gates [16–19]. This comes at the cost of a substantial overhead in runtime and qubit number, in particular if the connectivity between qubits is low. In superconducting qubit architectures, this has led to the development of problem-specific continuous two-qubit gate sets to partially reduce the overhead [11,12,20,21]. A complementary strategy is the direct use of multiqubit entangling operations, which can significantly enhance the efficiency to create large-scale entanglement. This strategy is employed in trapped ion systems with convincing demonstrations using common vibrational modes [22–24] and proposals using cavity-mediated interactions [25,26]. The challenge is, however, to design multiqubit operations that are fast and accurate when compared to an equivalent two-qubit gate decomposition, to avoid decoherence and reach high fidelities. For superconducting qubit architectures, several techniques for implementing multiqubit operations have been investigated, e.g., utilizing noncomputational qutrit states to implement more efficient digital decompositions [13,27–30], applying simultaneous pairwise couplings to generate effective multiqubit interactions [31–35], or introducing a shared coupling element acting as a multiqubit coupler [36–41]. Each approach comes with its specific advantages and challenges. For instance, implementations based on qutrit decomposition are easy to calibrate since they use existing gate types but may suffer from decoherence due to long periods spent in higher excited states. Simultaneous pairwise couplings can be implemented on

*niklas.glaser@wmi.badw.de

†stefan.filipp@wmi.badw.de

Published by the American Physical Society under the terms of the [Creative Commons Attribution 4.0 International](https://creativecommons.org/licenses/by/4.0/) license. Further distribution of this work must maintain attribution to the author(s) and the published article's title, journal citation, and DOI.

existing architectures but may be limited by low effective interaction strengths and spurious qubit interactions. And shared coupling elements provide high connectivity, but exhibit unwanted interaction terms caused by frequency crowding.

In this work we investigate a system of three transmon-type qubits coupled via a shared transmon-type coupler, which is tunable in frequency via an external flux. Previous work has shown that two-qubit controlled-phase (CPHASE) gates can be realized by controlling the frequency of the tunable coupler [42–46]. Here, we extend this scheme to a three-qubit system, and demonstrate that two- and three-body interaction terms can be utilized to implement the full family of controlled-controlled-phase (CCPHASE) and simultaneous pairwise CPHASE gates. These effective interactions are activated by adiabatic flux pulses and originate from conditional energy shifts due to hybridizations of qubit and coupler states within the same excitation manifold. To control the acquired two- and three-qubit phases, we devise a flexible refocusing scheme. Therefore, strong couplings between the qubits and the tunable coupler are utilized to realize fast entangling gates with a low population in higher excited states and a large on:off coupling ratio.

II. DESCRIPTION OF THE SYSTEM

We consider three fixed-frequency transmon-type [47] qubits (Q_1 , Q_2 , Q_3), coupled via a frequency-tunable coupler [42,48–50] (see Fig. 1) described by the Hamiltonian

$$H_{\text{sys}} = H_0 + H_{\text{int}} + H_{\text{drive}}, \quad (1)$$

where

$$\begin{aligned} H_0 &= \sum_{i=1,2,3} \omega_i \hat{a}_i^\dagger \hat{a}_i + \frac{\alpha_i}{2} \hat{a}_i^\dagger \hat{a}_i^\dagger \hat{a}_i \hat{a}_i + \omega_c(\Phi_{\text{ext}}) \hat{a}_c^\dagger \hat{a}_c \\ &\quad + \frac{\alpha_c}{2} \hat{a}_c^\dagger \hat{a}_c^\dagger \hat{a}_c \hat{a}_c, \\ H_{\text{int}} &= \frac{1}{2} \sum_{i \in \{1,2,3,c\}} \sum_{j \neq i} g_{ij} (\hat{a}_i^\dagger - \hat{a}_i) (\hat{a}_j^\dagger - \hat{a}_j), \\ H_{\text{drive}} &= \sum_{i=1,2,3} \Omega_i(t) (\hat{a}_i^\dagger + \hat{a}_i), \end{aligned}$$

with $\hbar = 1$. Here H_0 is the Hamiltonian of the bare uncoupled system with creation (annihilation) operators \hat{a}_i^\dagger (\hat{a}_i), frequencies ω_i , and anharmonicities α_i of the qubits and the coupler ($i = 1, 2, 3, c$). The coupler frequency ω_c can be tuned by applying an external flux Φ_{ext} . In the following we assume the experimentally realizable values $\omega_i/2\pi = \{3.5, 4, 4.5, 4.5 - 5.8\}$ GHz and $\alpha_i/2\pi = \{-200, -230, -200, -300\}$ MHz. We define the bare basis with the eigenstates $|n_c, n_1 n_2 n_3\rangle^0$ of H_0 , where

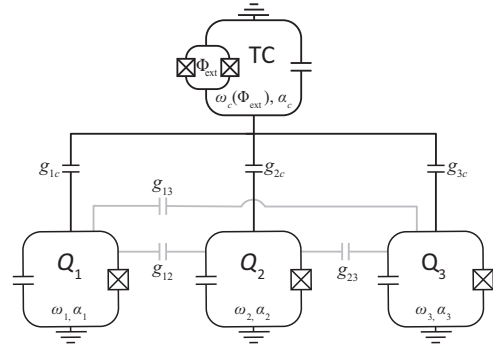


FIG. 1. Circuit representation of the fixed-frequency transmon-type qubit setup. Qubits Q_1 , Q_2 , and Q_3 with frequencies ω_i and anharmonicities α_i are capacitively coupled to a flux- (Φ_{ext}) -tunable coupler (TC) with frequency ω_c and anharmonicity α_c . The couplings g_{ic} between the qubits and the coupler are assumed to be larger than the stray capacitive couplings g_{ij} between qubits (gray lines).

n_i is the excitation number of element i . The interaction Hamiltonian H_{int} models the capacitive couplings between the elements, for which we choose $g_{ic}/2\pi = \{150, 150, 120\}$ MHz between qubits Q_i and the tunable coupler and stray direct qubit-qubit couplings $g_{i,i+1}/2\pi = \{13, 14, 10\}$ MHz, which are an order of magnitude smaller. The term H_{drive} models microwave drives on qubits Q_i with respective Rabi rates $\Omega_i(t)$. At idle times and for single-qubit operations, the coupler frequency $\omega_{c,\text{idle}}/2\pi = 5.8$ GHz is chosen to lie above the qubit frequencies where the effective coupling between the qubits is minimized [51]. Tuning the coupler frequency close to the qubit frequencies leads to energy shifts and enhanced interaction strengths between the qubits [42], as shown in the energy-level diagram in Fig. 2(a). To describe the protocol based on adiabatically modifying the frequency of the tunable coupler, we use the notation $|n_1 n_2 n_3\rangle(\omega_c)$ for an instantaneous eigenstate of the system within the $(n_1 + n_2 + n_3)$ -excitation manifold that is adiabatically connected to the initial state $|n_1 n_2 n_3\rangle(\omega_{c,\text{idle}}) \approx |0, n_1 n_2 n_3\rangle^0$ with zero excitations in the coupler. Since we are interested only in the dynamics in the qubit subspace, we diagonalize Hamiltonian (1) and restrict ourselves to the computational qubit states with zero excitations in the coupler. This results in the Hamiltonian

$$\tilde{H}_{\text{comp}} = \sum_{n_1, n_2, n_3 \in \{0,1\}} \tilde{\omega}_{n_1 n_2 n_3} |n_1 n_2 n_3\rangle \langle n_1 n_2 n_3|, \quad (2)$$

where $\tilde{\omega}_{n_1 n_2 n_3}$ are the instantaneous eigenfrequencies of the adiabatic states $|n_1 n_2 n_3\rangle$.

Tuning the coupler frequency close to the qubit frequencies results in avoided crossings and energy shifts of the adiabatic states. The first relevant avoided crossings occur when the tunable coupler and the qubit with the highest transition frequency (Q_3) become resonant

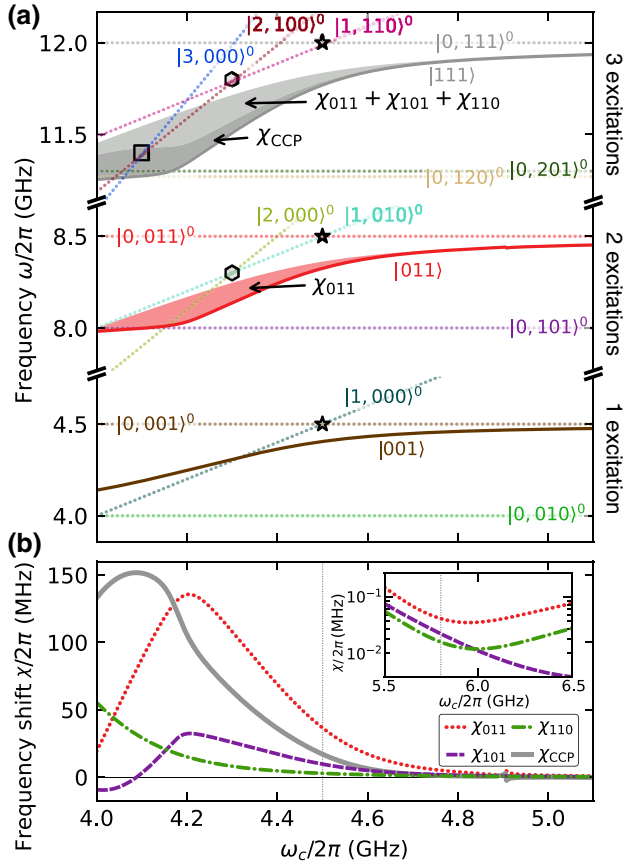


FIG. 2. (a) Energy-level diagram for selected states of the three-qubit system. Other states are discussed in Appendix B. The computational adiabatic states $|n_1n_2n_3\rangle$ (solid lines) and the bare states $|n_c, n_1n_2n_3\rangle^0$ (dotted lines) are shown in the single-, two-, and three-excitation manifolds as a function of ω_c . The frequencies ω of the states are given relative to the ground state $|0, 000\rangle^0$. Avoided crossings relevant to the adiabatic states are highlighted: $|1, n_1n_20\rangle^0 \leftrightarrow |0, n_1n_21\rangle^0$ (stars), $|2, n_100\rangle^0 \leftrightarrow |1, n_110\rangle^0$ (hexagons), and $|3, 000\rangle^0 \leftrightarrow |2, 100\rangle^0$ (square). The red shaded area represents the shift χ_{011} of $|011\rangle$ from the sum of the frequencies of the respective single-excitation states. The gray shaded areas represent the equivalent shift χ_{111} of $|111\rangle$ with contributions from two-qubit terms (light gray) and from a three-qubit term χ_{CCP} (dark gray). The frequency shifts are calculated according to Eqs. (3), after numerical diagonalization. (b) Energy shifts χ as a function of ω_c . Pink, red, and purple solid lines show two-qubit frequency shifts and the gray line shows the three-qubit frequency shift χ_{CCP} . Light gray vertical line shows the operating point of the coupler. The inset shows the frequency shifts near the idling point at 5.8 GHz (vertical line) on a logarithmic scale. The three-qubit frequency shift χ_{CCP} lies below the displayed range.

($\omega_c = \omega_3$). These crossings, denoted by stars in Fig. 2, occur for all adiabatic states with one excitation in Q_3 , i.e., $|001\rangle, |011\rangle, |101\rangle$ (not shown), and $|111\rangle$. Lowering the coupler frequency further leads to a hybridization and an energy shift χ_{011} on $|011\rangle$ when the second excited state

of the coupler $|2, 000\rangle^0$ and state $|1, 010\rangle^0$ become resonant ($\omega_c = \omega_2 - \alpha_c$), as denoted by the hexagon in Fig. 2. Similarly, state $|111\rangle$ in the three-excitation manifold is shifted in energy by χ_{011} due to the $|2, 100\rangle^0 \leftrightarrow |1, 110\rangle^0$ interaction. These additional energy shifts introduce a two-body interaction term between qubits Q_2 and Q_3 . Finally, the avoided crossing of the bare states $|3, 000\rangle^0$ and $|2, 100\rangle^0$, denoted by a square in Fig. 2, leads to a hybridization of the adiabatic state $|111\rangle$. The resulting energy shift χ_{CCP} introduces the targeted three-body interaction for implementing controlled-controlled-phase gates. We note that a negative coupler anharmonicity is required for the optimal succession of the avoided crossings for the generation of the discussed energy shifts. The relevant two- and three-qubit energy shifts are determined from the diagonalized Hamiltonian as

$$\chi_{011} = \tilde{\omega}_{011} - (\tilde{\omega}_{001} + \tilde{\omega}_{010}), \quad (3a)$$

$$\chi_{101} = \tilde{\omega}_{101} - (\tilde{\omega}_{001} + \tilde{\omega}_{100}), \quad (3b)$$

$$\chi_{110} = \tilde{\omega}_{110} - (\tilde{\omega}_{010} + \tilde{\omega}_{100}), \quad (3c)$$

$$\begin{aligned} \chi_{CCP} = & \tilde{\omega}_{111} - (\tilde{\omega}_{001} + \tilde{\omega}_{010} + \tilde{\omega}_{100}) \\ & - (\chi_{011} + \chi_{101} + \chi_{110}). \end{aligned} \quad (3d)$$

Tuning the coupler frequency close to the aforementioned avoided crossings results in large shifts of $\chi_{CCP} > 150$ MHz and $\chi_{011} > 120$ MHz [see Fig. 2(b)]. We choose the coupler frequency for gate operation at $\omega_c^{\text{op}}/2\pi = 4.5$ GHz to balance the magnitude of the energy shifts and the population losses due to nonadiabatic effects of the flux pulses; however, the optimal working points for idling and gate operations depend on the specific Hamiltonian parameters.

At the idling position $\omega_{c,\text{idle}}$ only minimal energy shifts, below 80 kHz, arise [see the inset of Fig. 2(b)].

To describe the entangling action of Hamiltonian \tilde{H} , we switch to a frame rotating at the individual qubit frequencies:

$$\tilde{H} = \chi_{011}H_{23} + \chi_{101}H_{13} + \chi_{110}H_{12} + \chi_{CCP}H_{CCP} \quad (4)$$

with the two-qubit CPHASE $_{kl}$ terms $H_{kl} = |11\rangle_{kl}\langle 11|_{kl}$ acting on the qubit subspace Q_k and Q_l , and a three-qubit CCPHASE term $H_{CCP} = |111\rangle\langle 111|$. In experiments this frame rotation corresponds to applying single-qubit Z-phase gates [52]. In this frame, an evolution under \tilde{H} corresponds to a combination of CPHASE and CCPHASE gates

$$\begin{aligned} & U(\phi_{011}, \phi_{101}, \phi_{110}, \phi_{CCP}) \\ & = \exp\left(-i \int_0^\tau \tilde{H}(t) dt\right) \\ & = \text{CPHASE}_{12}(\phi_{110}) \times \text{CPHASE}_{13}(\phi_{101}) \\ & \quad \times \text{CPHASE}_{23}(\phi_{011}) \times \text{CCPHASE}(\phi_{CCP}) \end{aligned} \quad (5)$$

with the entangling phases

$$\phi_j = - \int_0^\tau \chi_j dt \quad \text{for } j \in \{001, 101, 110, \text{CCP}\}. \quad (6)$$

III. MULTIQUBIT GATES BY HAMILTONIAN REFOCUSING

To implement a pure CPHASE(ϕ_{CCP}) gate without two-qubit CPHASE contributions, the conditions $\phi_{011} = k 2\pi$, $\phi_{101} = l 2\pi$, $\phi_{110} = m 2\pi$ for Eq. (6) need to be fulfilled with integers k, l, m . However, using only the external flux applied on the coupler as a control parameter, the gate duration is bounded from below by the time needed to accumulate at least a phase of 2π on all states. Additionally, matching all phases may require complex trajectories or a greater time overhead. These problems can be resolved by utilizing a refocusing scheme [53–55], where the evolution under \tilde{H} is interleaved with single-qubit π pulses to permute the states accumulating the entangling phases. Effective two- and three-qubit gate Hamiltonians such as

$$H_{\text{eff}}^{kl} = \chi_{\text{eff}} H_{kl} \quad \text{and} \quad H_{\text{eff}}^{\text{CCP}} = \chi_{\text{eff}} H_{\text{CCP}} \quad (7)$$

can then be realized by choosing interaction times such that unwanted phase contributions cancel out, as discussed in the following.

A. Controlled-phase gate

To generate a two-qubit CPHASE gate, the noninteracting qubit needs to be dynamically decoupled [56,57] from the rest of the system so that only interactions between the other two qubits remain. As an example, we consider a CPHASE gate between Q_1 and Q_3 , for which two interaction periods of equal duration τ are interleaved with two π pulses on Q_2 (X_2), as shown in Fig. 3(a). The two π pulses alter the action of the second interaction Hamiltonian as

$$\begin{aligned} \tilde{H}^{\perp X_1} &= X_2 \tilde{H} X_2 \\ &\cong -\chi_{011} H_{23} + (\chi_{101} + \chi_{\text{CCP}}) H_{13} - \chi_{110} H_{12} \\ &\quad - \chi_{\text{CCP}} H_{\text{CCP}}, \end{aligned} \quad (8)$$

where “ \cong ” defines an equality that neglects global and single-qubit terms (see Appendix C for further details). In $\tilde{H}^{\perp X_1}$ the signs of all components are inverted except for H_{13} , which increases by χ_{CCP} . The action of the full CPHASE sequence is then given by

$$\begin{aligned} X_2 e^{-i\tau \tilde{H}} X_2 e^{-i\tau \tilde{H}} &= e^{-i\tau [\tilde{H}^{\perp X_1} + \tilde{H}]} \\ &= e^{-i\tau [2\chi_{101} + \chi_{\text{CCP}}] H_{13}} = \text{CPHASE}_{13}(\phi_{101}), \end{aligned} \quad (9)$$

where we have used the equality $U e^{-i\tilde{H}} U^{-1} = e^{-iU\tilde{H}U^{-1}}$ and the fact that the interaction Hamiltonians are diagonal

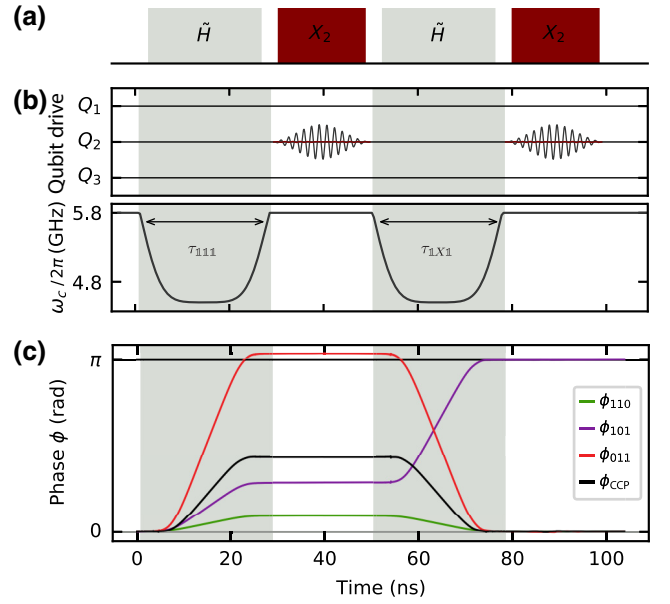


FIG. 3. Numerical simulation of a CPHASE $_{13}(\pi)$ gate between Q_1 and Q_3 . (a) The interaction Hamiltonian \tilde{H} is applied twice, interleaved by single-qubit π pulses on Q_2 . (b) Pulse sequence on Q_2 and the tunable coupler. Interactions are activated by tuning the coupler frequency ω_c , with 27-ns-long pulses. Single-qubit π rotations are implemented on Q_2 by 20-ns-long microwave pulses. (c) Instantaneous entangling phases during the pulse sequence. The final value of the collected phase of ϕ_{110} , ϕ_{011} , and ϕ_{CCP} is zero, while the value of ϕ_{101} is π , which realizes a CPHASE gate between Q_1 and Q_3 .

and, hence, commute with each other. This is equivalent to evolving for 2τ under the effective Hamiltonian (7) with $\chi_{\text{eff}} = \chi_{101} + \chi_{\text{CCP}}/2$ and $\phi_{101} = \tau[2\chi_{101} + \chi_{\text{CCP}}]$.

To verify the performance of the CPHASE gate, we numerically simulate the CPHASE $_{13}(\pi)$ gate resulting in a fidelity of 99.77% at a gate time of approximately 100 ns (see Appendix A for simulation details), assuming that decoherence times are much longer than gate times. To tune the coupler from its idle position $\omega_c^{\text{id}} = 5.8$ GHz to the operation point $\omega_c^{\text{op}} = 4.5$ GHz, we use rectangular pulses with Gaussian edges:

$$\omega_c(t) = \omega_c^{\text{id}} + (\omega_c^{\text{op}} - \omega_c^{\text{id}}) \text{erf}\left(\frac{t}{\tau_R}\right) \text{erf}\left(\frac{\tau - t}{\tau_R}\right). \quad (10)$$

Here $\tau = 27$ ns is the width of the pulse and erf is the Gaussian error function with a rise time characterized by $\tau_R = 5$ ns [Fig. 3(b)]. The π pulses are driven by a microwave pulse, with a 20 ns Gaussian envelope including a derivative-removal-by-adiabatic-gate [58] correction, with fidelities $> 99.96\%$. The numerically simulated evolution of the entangling phases is shown in Fig. 3(c). Initially, all entangling phases evolve at a positive rate. However, after the π pulse on Q_2 all accumulation rates are inverted except for ϕ_{110} , resulting in the desired entangling phases of $\phi_{110} = \phi_{011} = \phi_{\text{CCP}} = 0$ and

$\phi_{101} = \pi$. With this approach we can realize all pairwise two-qubit $\text{CPHASE}_{kl}(\phi_{kl})$ gates by performing interleaved π pulses on the qubit not participating in the gate. The effective Hamiltonians for the different combinations of enclosing π pulses are listed in Table I.

B. Controlled-controlled-phase gate

To implement a CCPHASE gate, the refocusing technique can be extended to four interaction periods interleaved with single-qubit π pulses on different qubits, as shown in Fig. 4(a). For the observed relation, $\chi_{101} > \chi_{\text{CCP}} > \chi_{110}$, we choose the permutations $\mathbb{1}\mathbb{1}\mathbb{1}$, $\mathbb{1}X\mathbb{1}$, $XX\mathbb{1}$, and $\mathbb{1}XX$. We skip repeated single-qubit π rotations that appear between permutations and thus apply six single-qubit gates in total. To find the correct duration of each flux pulse, we solve the system of equations

$$\begin{pmatrix} \phi_{23} + k_{23}2\pi \\ \phi_{13} + k_{13}2\pi \\ \phi_{12} + k_{12}2\pi \\ \phi_{\text{CCP}} + k2\pi \end{pmatrix} = \begin{pmatrix} \chi_{011} & -\chi_{011} & -\chi_{011} - \chi_{\text{CCP}} & \chi_{011} \\ \chi_{101} & \chi_{101} + \chi_{\text{CCP}} & -\chi_{101} - \chi_{\text{CCP}} & -\chi_{101} - \chi_{\text{CCP}} \\ \chi_{110} & -\chi_{110} & \chi_{110} & -\chi_{110} - \chi_{\text{CCP}} \\ \chi_{\text{CCP}} & -\chi_{\text{CCP}} & \chi_{\text{CCP}} & \chi_{\text{CCP}} \end{pmatrix} \begin{pmatrix} \tau_{\mathbb{1}\mathbb{1}\mathbb{1}} \\ \tau_{\mathbb{1}X\mathbb{1}} \\ \tau_{XX\mathbb{1}} \\ \tau_{\mathbb{1}XX} \end{pmatrix} \quad (11)$$

derived from the Hamiltonian coefficients in Table I, assuming a linear increase of entangling phases with the duration of the flux pulses (see Appendix D). As for the two-qubit CPHASE gate above, we simulate the coherent dynamics for a CCPHASE(π) gate, with pulse durations (55, 25, 65, 20) ns and plot the evolution of the entangling phases in Fig. 4(b). With these timings, we obtain final entangling phases of $\phi_{110} = 0$, $\phi_{011} = \phi_{101} = -2\pi$ and $\phi_{\text{CCP}} = 3\pi$ and a simulated fidelity of 99.58% in 245 ns including the single-qubit gates [see Fig. 4(c)]. Leakage caused by imperfectly adiabatic pulses is the main coherent error contribution, as discussed in Sec. IV.

C. Generalized controlled-controlled-phase gate

Applying the same refocusing scheme, Eq. (11) can be used to determine pulse durations that result in arbitrary two- and three-qubit entangling phases. This method therefore provides full control over all entangling phases and

TABLE I. Signs of the coefficients of the effective Hamiltonians in Eq. (4) after applying leading and trailing π pulses on the respective qubits denoted by an X ($\mathbb{1}$ denotes no pulse). Each Hamiltonian term H_{kl}, H_{CCP} has positive or negative coefficients from any of the conditional shifts $\chi_{011}, \chi_{101}, \chi_{110}, \chi_{\text{CCP}}$; empty cells denote vanishing coefficients. The implementation of the proposed CCPHASE gate makes use of the first four permutations in the table (light gray).

π pulses ($Q_1Q_2Q_3$)	H_{23}		H_{13}		H_{12}		H_{CCP}
	χ_{011}	χ_{CCP}	χ_{101}	χ_{CCP}	χ_{110}	χ_{CCP}	χ_{CCP}
$\mathbb{1}\mathbb{1}\mathbb{1}$	+		+		+		+
$\mathbb{1}X\mathbb{1}$	-		+	+	-		-
$XX\mathbb{1}$	-	-	-	-	+		+
$\mathbb{1}XX$	+		-	-	-	-	+
$\mathbb{1}\mathbb{1}X$	-		-		+	+	-
$X\mathbb{1}X$	-	-	+		-	-	+
$X\mathbb{1}\mathbb{1}$	+	+	-		-		-
XXX	+	+	+	+	+	+	-

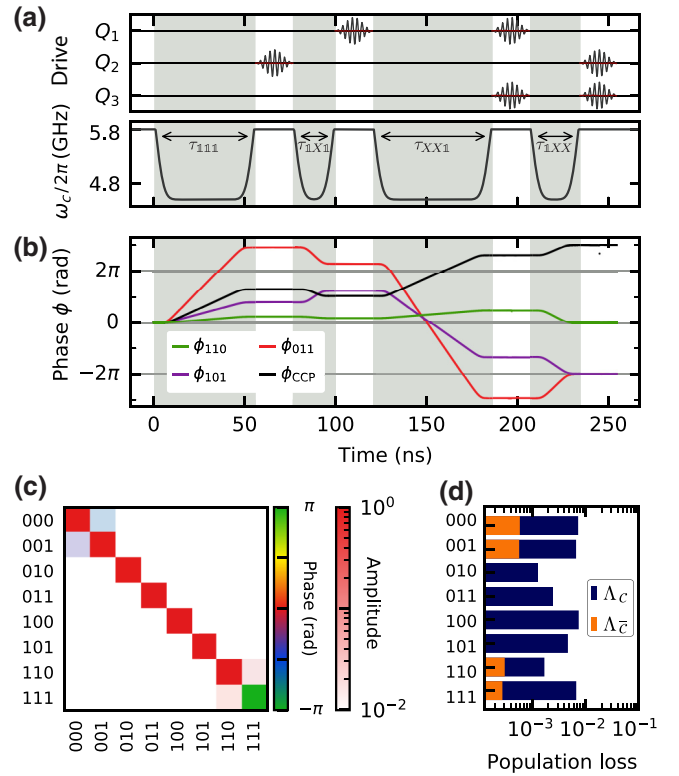


FIG. 4. Numerical simulation of a CCPHASE(π) gate. (a) Four independent adiabatic pulses modulate the frequency ω_c of the coupler, with durations $\tau_{\mathbb{1}\mathbb{1}\mathbb{1}}, \tau_{\mathbb{1}X\mathbb{1}}, \tau_{XX\mathbb{1}}, \tau_{\mathbb{1}XX}$. The coupler pulses are interleaved by single-qubit refocusing pulses, on the respective qubits Q_i . (b) Instantaneous entangling phases ϕ_i collected during the gate execution. (c) Propagator of the simulated gate. Phase and amplitude of matrix elements are represented in color and opacity, respectively. (d) Population loss from the initialized computational states after the gate execution to other computational states Λ_C (orange), equivalent to the sum of the squared off-diagonal elements in (c), or to states outside the computational basis $\Lambda_{\bar{C}}$ (blue).

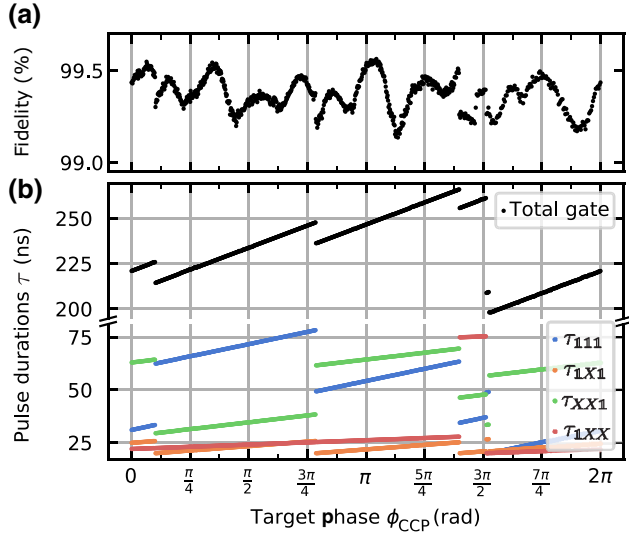


FIG. 5. Continuous CCPHASE(ϕ_{CCP}) gate with varying target phase ϕ_{CCP} . (a) Fidelity and (b) gate duration including single-qubit π pulses. Individual adiabatic pulse durations τ_i for realizing the respective target phases are shown with colored dots. The discontinuities are caused by the 2π -phase degree of freedom when solving Eq. (11).

directly allows for the implementation of the generalized three-qubit controlled-phase gate

$$\begin{aligned} U_{3Q\phi}(\phi_{12}, \phi_{13}, \phi_{23}, \phi_{CCP}) \\ = \text{CPHASE}_{12}(\phi_{12}) \times \text{CPHASE}_{13}(\phi_{13}) \\ \times \text{CPHASE}_{23}(\phi_{23}) \times \text{CCPHASE}(\phi_{CCP}), \end{aligned} \quad (12)$$

which corresponds to the simultaneous application of pairwise two- and three-qubit controlled-phase gates. In particular, we can implement a CCPHASE gate with an arbitrary angle ϕ_{CCP} . We numerically evaluate the gate fidelities and pulse durations for ϕ_{CCP} continuously varying between 0 and 2π , as shown in Fig. 5. We find that all phase combinations can be realized with total gate lengths between 195 and 270 ns. Without including decoherence, the fidelity for all implementation lies between 99.1%–99.6%, with oscillations due to periodic leakage effects (see Appendix D for more details). Similarly, $U_{3Q\phi}$ gates with arbitrary settings of both the two- and three-qubit phases ϕ_{ij} and ϕ_{CCP} result in gate times below 300 ns and gate fidelities above 99% (not shown).

IV. ERROR CONTRIBUTIONS

To assess the expected performance of the gate operations, we evaluate the error contributions from coherent errors and from decoherence on the CCPHASE(π) gate. The coherent errors of 0.42% are dominated by leakage, i.e., all population losses $\Lambda_s = \sum_{f \neq i} \langle f | U | i \rangle^2$ from computational states $|i\rangle \in \mathcal{C}$ to states outside the computational

subspace $|f\rangle \in s = \bar{\mathcal{C}}$ [blue bars in Fig. 4(d)], which are caused by imperfect adiabatic pulses. Transitions to other computational states $|f\rangle \in s = \mathcal{C} \setminus \{|i\rangle\}$ [orange bars in Fig. 4(d)] caused by imperfections in single-qubit gates are another coherent error source, leading to off-diagonal elements in the propagator [Fig. 4(c)]. For a single flux pulse, most of the losses occur from the states $|111\rangle$ and $|011\rangle$ (see Appendix D). However, permuting the states with the interleaved single-qubit pulses distributes the leakage over all computational states. Note that the coherent errors scale with the number of flux pulses. For the CPHASE gate, which uses two flux pulses, coherent errors amount to 0.23%, roughly a factor 2 smaller than that of the CCPHASE gate, which uses four.

In addition to leakage, decoherence of both qubits and the coupler will limit the achievable gate fidelities. In particular, because of the transmon-type tunable coupler, charge noise may induce errors due to the hybridization in higher-excitation manifolds. We therefore simulate the open-system dynamics of the system by solving the time-evolution under the Lindblad master equation

$$\dot{\rho} = -i[H, \hat{\rho}(t)] + \sum_k \left(\hat{L}_k \hat{\rho} \hat{L}_k^\dagger - \frac{1}{2} \left\{ \hat{L}_k^\dagger \hat{L}_k, \hat{\rho}(t) \right\} \right) \quad (13)$$

with Hamiltonian H , density matrix ρ , and collapse operators \hat{L}_k accounting for relaxation and dephasing. We assume that the relaxation rates that are linearly increasing with excitation number $\Gamma_1^{(m+1,m)} = m/T_1$, where $\Gamma_1^{(j,m)}$ is the decay rate from state $|j\rangle$ to state $|m\rangle$, and T_1 is the relaxation time of the first excited state [47,59]. The pure dephasing rate $\Gamma_\phi^{(m)} = \Gamma_{\phi,c}^{(m)} + \Gamma_{\phi,e}^{(m)}$ between states $|m\rangle$ and $|m+1\rangle$ is modeled as the sum of a constant term $\Gamma_{\phi,c}^{(m)} = 1/T_\phi$ and an energy-level-dependent term $\Gamma_{\phi,e}^{(m)}$ incorporating charge noise [47,60,61]. We account for a charge noise dephasing rate $\Gamma_{\phi,n}^{(m)} = \pi A_n |\epsilon_m|$ given the charge noise strength A_n and the approximated charge dispersion amplitude [47]

$$\epsilon_m \simeq (-1)^m E_C \frac{2^{4m+5}}{m!} \sqrt{\frac{2}{\pi}} \left(\frac{E_J}{2E_C} \right)^{m/2+3/4} e^{-\sqrt{8E_J/E_C}}. \quad (14)$$

We assume equal decoherence rates on all qubits and couplers. Although flux-tunable transmons tend to have higher dephasing rates due to their sensitivity to flux noise, this can be mitigated by introducing a coupler with an asymmetric superconducting quantum interference device [47] and choosing idling and operating points to be at the flux sweetspots.

We determine the individual contributions of each error channel by comparing the simulations with the respective error channel turned on and off. We find that the errors

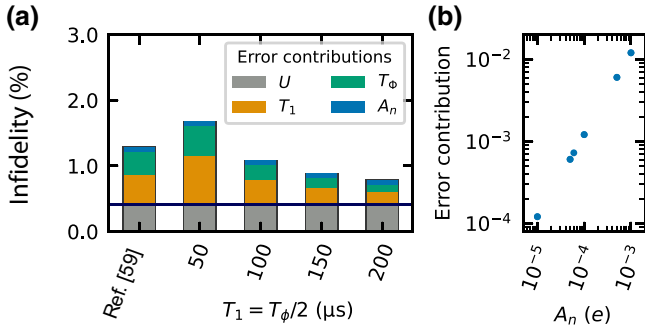


FIG. 6. Effect of coherent errors and decoherence on CCPHASE gate fidelities. (a) The infidelity of the numerically simulated CCPHASE gate for different relaxation times T_1 and pure dephasing times T_ϕ . The first bar shows the results of a model according to Ref. [59]. Different colors denote the contributions of the respective error channels: coherent errors U (gray), T_1 relaxation (orange), pure T_ϕ dephasing (green), and charge noise A_n errors (blue). (b) Error contribution from charge noise for various noise strengths A_n .

are independent of each other and can be linearly added. Using typical values of $T_1 = 84$ μ s, $T_\phi = 124$ μ s, and $A_n = 6 \times 10^{-5}e$ (see, e.g., Peterer *et al.* [59]), we obtain a total CCPHASE(π) gate infidelity of 1.30%, as compared to only coherent errors of 0.42%, as shown in Fig. 6(a). Keeping the noise amplitude fixed, we evaluate infidelities for varying values of T_1 and T_ϕ , assuming that, as the coherence times improve, the ratio between them will remain approximately $T_1 = T_\phi/2$. For $T_1 = 50$ μ s, we find that decoherence is the dominant contribution; however, for state-of-the-art coherence times $T_1 > 100$ μ s [62,63], decoherence and coherent errors become comparable, with total errors of approximately 1% and below. The error caused by charge noise with a typical strength $A_n = 6 \times 10^{-5}e$ [59,64] is expected to be below 0.1%, with the error scaling roughly linearly with the charge noise amplitude, as shown in Fig. 6(b).

V. DISCUSSION AND OUTLOOK

In summary, we propose a system of three qubits coupled via a shared tunable coupler and develop a pulse scheme that implements generalized three-qubit controlled-phase gates. Adiabatic flux pulses allow us to tune the two- and three-body interaction strengths. The resulting entangling phases are controlled by interleaving interaction periods with single-qubit refocusing pulses. With this method, we show in numerical simulations that three-qubit controlled-controlled-phase gates can be realized in less than 300 ns with fidelities above 99% for all desired entangling phases when the effects of decoherence can be ignored. Taking realistic values for qubit and coupler coherence times into account, we expect an added gate error below 1%. Recent implementations of

three-qubit gates include cross-resonance-type i Toffoli gates [31] with fidelities of 98.3% in 353 ns, simultaneous parametric drive gates [65] with fidelities of 97.9% in 250 ns, Mølmer-Sørensen-type gates [39] with fidelities of 90.5% in 217 ns, and decomposed CCPHASE gates [13] with fidelities of 87.1% in 402 ns. By directly utilizing the strong qubit-coupler interactions and a flexible pulse scheme, the proposed CCPHASE gate has the potential to improve both speed and fidelity as compared to these recent realizations of three-qubit gates on superconducting qubits. Moreover, the studied three-qubit coupler refocusing scheme allows for the implementation of pairwise controlled-phase gates with adjustable phases, thus providing greater connectivity and flexibility in comparison to two-qubit couplers.

The proposed protocol can be modified in a number of ways to account for different experimental conditions. In the presence of strong charge noise the operating point of the coupler ω_c^{op} could be lowered, thus reducing charge noise sensitivity at the cost of longer gate times. Furthermore, the refocusing scheme can be adapted to result in a net-zero total applied flux, a technique known to reduce sensitivity to long-term correlated flux noise if present [61]. To reduce leakage errors, flux pulses could be individually optimized to harness destructive interference between multiple transitions [66] and ensure local adiabaticity [67]. In general, a refocusing scheme similar to that presented can be applied in other superconducting qubit architectures. For example, in systems with two-qubit couplers and simultaneous interactions [32] it could provide greater control of all interaction terms and shorter gate durations. Moreover, the number of qubits connected to the coupler could be increased further, allowing for strong and controllable many-body Hamiltonians with application in variational algorithms and Hamiltonian simulations. Finally, in the context of quantum applications, the investigated architecture is a promising candidate for the implementation of variational algorithms designed to solve optimization problems. In particular, the problem Hamiltonian for MAX-3-SAT problems can be directly implemented by the generalized controlled-phase gate, providing an improvement in speed and accuracy over a gate decomposition into single- and two-qubit gates.

ACKNOWLEDGMENTS

We thank Ivan Tsitsilin, Gerhard Huber, and Franz Haslbeck for insightful discussions. We acknowledge funding from the European Commission Marie Curie ETN project QuSCo (Grant No. 765267), from the German Federal Ministry of Education and Research via the funding program “Quantum Technologies-From Basic Research to the Market” (project GeQCoS) under Contract No. 13N15680, and from the European FET-OPEN project Quomorphic (Grant No. 828826). We

also acknowledge funding by the Deutsche Forschungsgemeinschaft (DFG, German Research Foundation) under Project No. FI2549/1-1. We further acknowledge support by the Leibniz Supercomputing Centre, providing computing time on its Linux-Cluster.

APPENDIX A: SIMULATIONS

The density matrix dynamics are simulated with the q-optimize [68] package, using time-ordered piecewise exponentiation of Hamiltonian H_{sys} in Eq. (1). The dynamics are sampled at a rate of 30 GS/s, while the control signals are sampled at 2.4 GS/s with additional Gaussian filtering according to the specifications of a typically used arbitrary waveform generator, such as the HDAWG from Zurich Instruments [69]. We restrict the energy of the bare states to $E/(2\pi) = \omega_{\text{th}}/2\pi = 16$ GHz and therefore take only the lowest-lying energy levels of the qubits (4, 4, 3 for Q_1, Q_2, Q_3) and the tunable coupler (5) into account. We further truncate the Hilbert space to allow only up to four excitations in the system.

APPENDIX B: INTERACTING ENERGY LEVELS

While in Sec. II we discussed only the avoided crossings dominantly contributing to the energy shifts of states $|011\rangle$ and $|111\rangle$, here we extend the discussion to all crossings affecting the adiabatic computational states $|n_1 n_2 n_3\rangle, n_k \in \{0, 1\}$, as shown in Fig. 7.

The energy shift for the adiabatic state $|111\rangle$ occurs due to hybridization first with the $|1, 110\rangle^0$ state, then with $|2, 100\rangle^0$, and finally with $|3, 000\rangle^0$ [star, circle, and square,

respectively, in Fig. 7(c)]. Likewise, the energy shift for the adiabatic state $|011\rangle$ occurs due to hybridization first with the $|1, 010\rangle^0$ state and then with $|2, 000\rangle^0$ [top star and circle, respectively, in Fig. 7(b)]. In both situations, lowering the coupler frequency ω_c past the last transition should further increase the energy shifts. However, this behavior is inhibited by hybridization with other bare states, such as $|0, 101\rangle^0$ for χ_{110} and $|0, 201\rangle^0, |0, 120\rangle^0$ for χ_{CCP} . At a higher coupler frequency, instead, two further avoided crossings affect the $|111\rangle$ and $|011\rangle$ states when tuning the coupler into the interaction area: $|1, 200\rangle^0 \leftrightarrow |0, 111\rangle^0$ and $|1, 100\rangle^0 \leftrightarrow |0, 011\rangle^0$, respectively. These avoided crossings have a gap of only a few megahertz, as both are caused by four-photon transitions, and therefore need to be passed diabatically, i.e., with a fast passage. For the choice of circuit parameters, it is thus essential to ensure that these four-photon crossings are located at a tunable coupler frequency ω_c above the idling point and separated from the chosen interaction area, such that the requirements on adiabaticity as well as diabaticity can both be fulfilled.

Similarly to $|011\rangle$, the adiabatic state $|101\rangle$ would experience a conditional energy shift χ_{101} due to hybridization first with the $|1, 100\rangle^0$ state [lower star in Fig. 7(b)] and then with $|2, 000\rangle^0$ (not shown), and the adiabatic state $|110\rangle$ would experience a conditional energy shift χ_{110} due to hybridization first with the $|1, 100\rangle^0$ state [triangle in Fig. 7(b)] and then with $|2, 000\rangle^0$ (not shown). However, the interaction with $|2, 000\rangle^0$ occurs at a coupler frequency $\omega_c = \omega_1 - \alpha_c$ below all qubit frequencies, making it difficult to reach areas with large energy shifts without causing

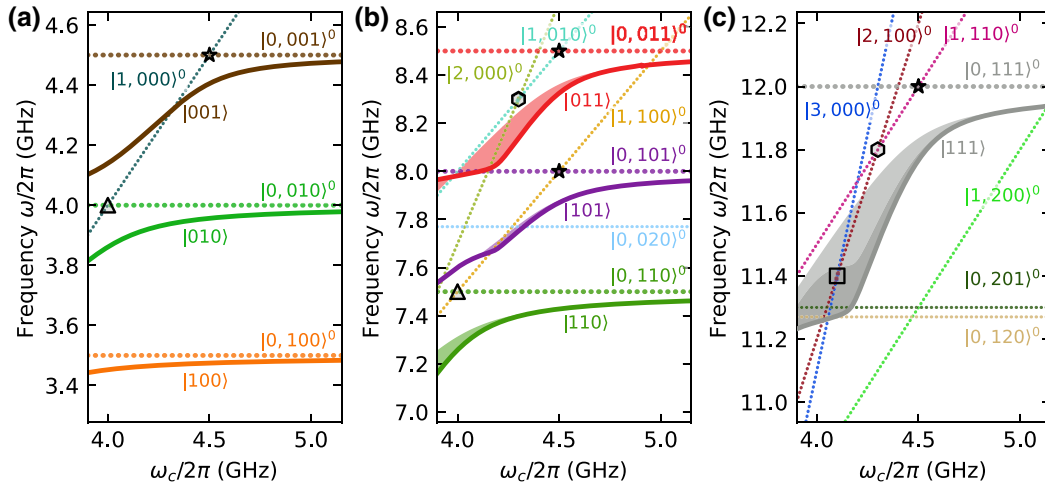


FIG. 7. Energy-level diagram of the three-qubit system. Frequencies with respect to the ground state $|0, 000\rangle$ of bare states (dotted lines) and adiabatic states (solid lines) are shown as a function of the coupler frequency, in the single- (a), double- (b), and triple-excitation (c) manifolds. The adiabatic states follow the eigenstates, except for avoided crossings with a gap spacing less than 10 MHz, assuming that those avoided crossings are passed diabatically. The coupler is idling at 5.8 GHz, defining the labeling of the adiabatic states. The relevant avoided crossings are marked as follows: star, $|1, n_1 n_2 0\rangle^0 \leftrightarrow |0, n_1 n_2 1\rangle^0$; hexagon, $|2, n_1 00\rangle^0 \leftrightarrow |1, n_1 10\rangle^0$; square, $|3, 000\rangle^0 \leftrightarrow |2, 100\rangle^0$; triangle, $|1, n_1 0 n_3\rangle^0 \leftrightarrow |0, n_1 1 n_3\rangle^0$.

leakage in at least some of the computational states. Even then, for the adiabatic state $|101\rangle$, a previous hybridization with the $|0,020\rangle^0$ state suppresses the energy shift χ_{101} and introduces the risk of leakage. Therefore, large energy shifts are only achievable on states $|011\rangle$ and $|111\rangle$.

APPENDIX C: METHOD OF REFOCUSING

By interleaving π pulses in the conditional phase accumulation, unwanted phase terms can be canceled to realize CPHASE and CCPHASE gates. Here we consider the interaction Hamiltonian [see also Eq. (4) in the main text]

$$\tilde{H} = \chi_{011}H_{23} + \chi_{101}H_{13} + \chi_{110}H_{12} + \chi_{CCP}H_{CCP}. \quad (C1)$$

Applying a leading and a trailing π - X pulse on Q_2 (X_2) results in \tilde{H}^{1X1} , which can be used in conjunction with \tilde{H} to realize a controlled-phase gate between Q_1 and Q_3 . A straightforward extension of this scheme to other qubit combinations results in the effective Hamiltonians listed in Table I.

The effective Hamiltonian \tilde{H}^{1X1} is given by

$$X_2 e^{-i\tilde{H}\tau} X_2 = e^{-iX_2 \tilde{H} X_2 \tau} = e^{-i\tilde{H}^{1X1} \tau}, \quad (C2)$$

where the first equality is given by $X_2 X_2 = \mathbb{1}$. The transformed Hamiltonian terms are then given by

$$\begin{aligned} H_{13}^{1X1} &= X_2 H_{13} X_2 \cong H_{13}, \\ H_{12}^{1X1} &= X_2 H_{12} X_2 \cong -H_{12}, \\ H_{23}^{1X1} &= X_2 H_{23} X_2 \cong -H_{23}, \\ H_{CCP}^{1X1} &= X_2 H_{CCP} X_2 \cong -H_{CCP} + H_{13}, \end{aligned}$$

using the relation $X_j Z_j X_j = -Z_j$ and the Hamiltonian terms

$$\begin{aligned} H_{kl} &= |11\rangle_{kl} \langle 11|_{kl} \\ &= (\mathbb{1}_k \mathbb{1}_l - \mathbb{1}_k Z_l + Z_k \mathbb{1}_l + Z_k Z_l)/4 \\ &\cong Z_k Z_l / 4, \end{aligned} \quad (C3a)$$

$$\begin{aligned} H_{CCP} &= |111\rangle \langle 111| \\ &= (\mathbb{1}\mathbb{1}\mathbb{1} - \mathbb{1}\mathbb{1}Z - \mathbb{1}Z\mathbb{1} - Z\mathbb{1}\mathbb{1} + ZZ\mathbb{1} \\ &\quad + Z\mathbb{1}Z + \mathbb{1}ZZ - ZZZ)/8 \\ &\cong (ZZ\mathbb{1} + Z\mathbb{1}Z + \mathbb{1}ZZ - ZZZ)/8, \end{aligned} \quad (C3b)$$

written in terms of the Pauli operators I and Z . Here we neglect global and single-qubit terms, denoted by “ \cong ” in Eqs. (C3). The resulting effective Hamiltonian is then given by

$$\begin{aligned} \tilde{H}^{1X1} &\cong -\chi_{011}H_{23} + (\chi_{101} + \chi_{CCP})H_{13} - \chi_{110}H_{12} \\ &\quad - \chi_{CCP}H_{CCP}. \end{aligned} \quad (C4)$$

APPENDIX D: OPTIMIZATION OF PULSE PARAMETERS

To maximize the gate fidelity, we investigate the effect of control parameters on the system dynamics, specifically, the accumulated phase during a flux pulse and the associated leakage. The flat-top pulse tuning the coupler from the idling to the interaction region is described by Eq. (10) with a rise-fall parameter $\tau_R = 5$ ns, a pulse length τ , and the operation point ω_c^{op} . Varying the pulse length τ linearly increases the accumulated phases ϕ_j [Eq. (6)], as shown in Fig. 8(a). Fitting this phase with a linear function provides the effective energy shifts χ_j used in Eq. (11), plus an offset given by the leading and trailing ramps. The population losses $\Lambda_{n_1 n_2 n_3}$ from the adiabatic states $|n_1 n_2 n_3\rangle$ remain approximately constant as a function of the pulse duration,

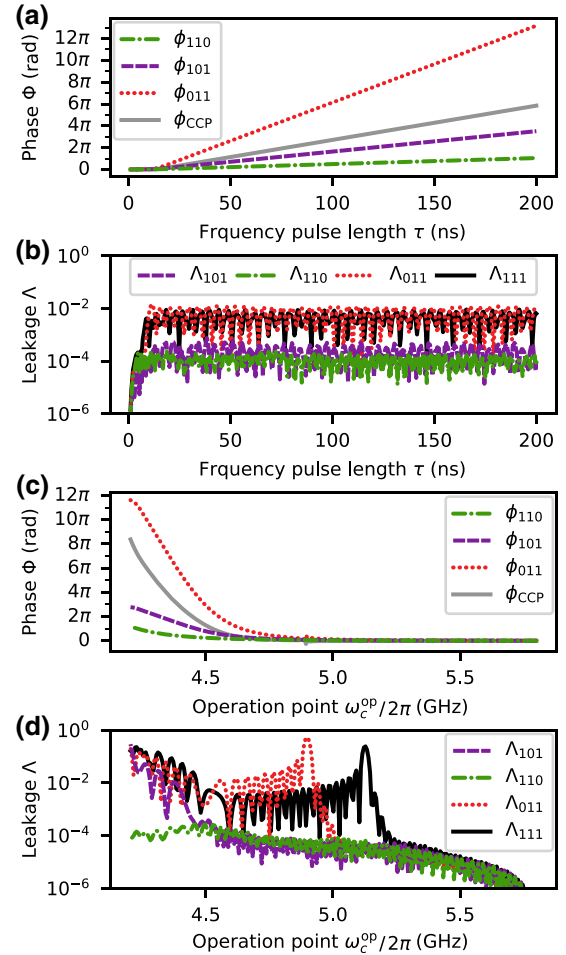


FIG. 8. Simulated entangling phases ϕ_j and individual state population loss $\Lambda_{n_1 n_2 n_3}$ as a function of gate duration τ (a),(b) and of coupler operating point frequency ω_c^{op} (c),(d). For all simulations, a half-Gaussian-square pulse is used, with total duration $\tau = 60$ ns, rise time $\tau_R = 5$ ns, and $\omega_c^{\text{op}} = 4.5$ GHz, unless otherwise specified. Model parameters are identical to those used in the main text.

with oscillations due to Landau-Zener-Stückelberg interference [66], suggesting that leakage is introduced only during the ramps of the pulse and not while in the interaction region [see Fig. 8(b)]. With this pulse, the slope of the ramp and thus its adiabaticity can be tuned by the rise-fall parameter τ_R . Individual pulses could be optimized to significantly suppress leakage by enforcing local adiabaticity, as well as utilizing destructive Landau-Zener-Stückelberg interference [61,70]. Varying, instead, the operation point ω_c^{op} for a pulse with fixed duration $\tau = 55$ ns will affect the magnitudes of the energy shifts so that lower ω_c^{op} leads to larger accumulated phases, as shown in Fig. 8(c). When choosing ω_c^{op} close to the four-photon avoided crossings $|1, 200\rangle^0 \leftrightarrow |0, 111\rangle^0$ and $|1, 100\rangle^0 \leftrightarrow |0, 011\rangle^0$, the involved states experience strong population losses [see Fig. 8(d)]. Instead, an operation point detuned from these crossings results in an improved diabatic passage and thus reduced leakage. Indeed, the results presented in the main text use an operation point near Q_3 ($\omega_c^{\text{op}} \approx \omega_3 = 4.5$ GHz), where we find a trade-off between low leakage and significant amounts of accumulated phase. Lowering the coupler frequency below this point leads to very strong hybridizations between states with excitations in the coupler and states with excitations in Q_3 , which would experience more leakage.

APPENDIX E: OPTIMIZATION OF DESIGN PARAMETERS

In optimizing design parameters we aim to maximize the strength of the energy shifts, which determines the gate speed, and minimize the amount of flux pulse leakage, which represents the dominant contribution of coherent errors. We limit our investigation to the coupling strengths g_{ic} between qubits and coupler and the anharmonicity α_c of the tunable coupler, as these will determine the width and position of the avoided crossings relevant for the gate [see Appendix B].

We find that the conditional energy shifts χ_j , as determined by Hamiltonian diagonalization, increase with increasing coupling strengths g_{ic} due to a greater energy gap of the avoided crossing [see Fig. 9(a)]. However, numerical simulation of the total final leakage $\Lambda = \sum_{n_1, n_2, n_3} \Lambda_{n_1 n_2 n_3}$ as a function of the coupling strengths g_{ic} exhibits nonmonotonic behavior, with oscillations due to Landau-Zener-Stückelberg interference [66], and a stable minimum around $g_{ic} \sim 120$ MHz [see Fig. 9(b)]. For smaller coupling strengths g_{ic} , the avoided crossings with excited coupler states become too narrow to be passed adiabatically and, for larger coupling strengths g_{ic} , the avoided crossings that should be passed diabatically become too wide to do so.

Increasing the magnitude of the anharmonicity of the coupler α_c brings the three main avoided crossings introducing energy shifts closer together. Therefore, the energy

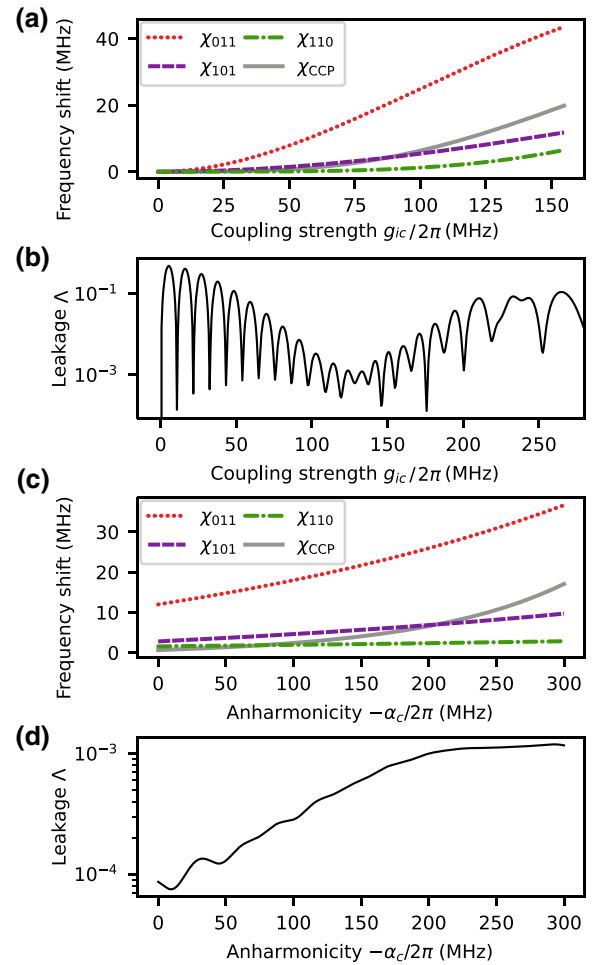


FIG. 9. Frequency shifts and leakage as a function of coupling strength and anharmonicity α_c . (a) Two-qubit energy shifts $\chi_{n_1 n_2 n_3}$ and the three-qubit energy shift χ_{CCP} as well as (b) leakage Λ after a flux pulse as a function of the coupling strength g_{ic} . (c) Energy shifts and (d) leakage as a function of the coupler anharmonicity α_c . The energy shifts are calculated at $\omega_c/2\pi = 4.5$ GHz. For the leakage simulation, a half-Gaussian-square pulse is used, with total duration $\tau = 60$ ns, rise time $\tau_R = 5$ ns, and $\omega_c^{\text{op}} = 4.5$ GHz. Other model parameters are identical to those used in the main text.

shifts at an operation point, here $\omega_c^{\text{op}} \approx 4.5$ GHz, increase as a function of $-\alpha_c$, as shown in Fig. 9(c). The stronger energy shifts come at the cost of more simultaneous hybridizations and frequency crowding, which increase the amount of leakage [Fig. 9(d)]. Nonetheless, the introduced leakage is limited to approximately 10^{-3} and the choice of anharmonicity will be mostly guided by charge noise considerations for transmon qubits.

[1] M. Kjaergaard, M. E. Schwartz, J. Braumüller, P. Krantz, J. I. Wang, S. Gustavsson, and W. D. Oliver, Superconducting

- qubits: Current state of play, *Annu. Rev. Condens. Matter Phys.* **11**, 369 (2020).
- [2] F. Arute, K. Arya, R. Babbush, D. Bacon, J. C. Bardin, R. Barends, R. Biswas, S. Boixo, F. G. S. L. Brandao, and D. A. Buell, *et al.*, Quantum supremacy using a programmable superconducting processor, *Nature* **574**, 505 (2019).
- [3] P. Jurcevic, A. Javadi-Abhari, L. S. Bishop, I. Lauer, D. F. Bogorin, M. Brink, L. Capelluto, O. Günlük, T. Itoko, and N. Kanazawa, *et al.*, Demonstration of quantum volume 64 on a superconducting quantum computing system, *Quantum Sci. Technol.* **6**, 025020 (2021).
- [4] G. J. Mooney, G. A. L. White, C. D. Hill, and L. C. L. Hollenberg, Whole-device entanglement in a 65-qubit superconducting quantum computer, *Adv. Quantum Technol.* **4**, 2100061 (2021).
- [5] M. Gong, S. Wang, C. Zha, M.-C. Chen, H.-L. Huang, Y. Wu, Q. Zhu, Y. Zhao, S. Li, and S. Guo, *et al.*, Quantum walks on a programmable two-dimensional 62-qubit superconducting processor, *Science* **372**, 948 (2021).
- [6] J. Preskill, Quantum computing in the NISQ era and beyond, *Quantum* **2**, 79 (2018).
- [7] A. Kandala, A. Mezzacapo, K. Temme, M. Takita, M. Brink, J. M. Chow, and J. M. Gambetta, Hardware-efficient variational quantum eigensolver for small molecules and quantum magnets, *Nature* **549**, 242 (2017).
- [8] A. Peruzzo, J. McClean, P. Shadbolt, M.-H. Yung, X.-Q. Zhou, P. J. Love, A. Aspuru-Guzik, and J. L. O'Brien, A variational eigenvalue solver on a photonic quantum processor, *Nat. Commun.* **5**, 1 (2014).
- [9] N. Moll, P. Barkoutsos, L. S. Bishop, J. M. Chow, A. Cross, D. J. Egger, S. Filipp, A. Fuhrer, J. M. Gambetta, and M. Ganzhorn, *et al.*, Quantum optimization using variational algorithms on near-term quantum devices, *Quantum Sci. Technol.* **3**, 030503 (2018).
- [10] F. Arute, *et al.*, Hartree-Fock on a superconducting qubit quantum computer, *Science* **369**, 1084 (2020).
- [11] M. Ganzhorn, D. Egger, P. Barkoutsos, P. Ollitrault, G. Salis, N. Moll, M. Roth, A. Fuhrer, P. Mueller, S. Woerner, I. Tavernelli, and S. Filipp, Gate-Efficient Simulation of Molecular Eigenstates on a Quantum Computer, *Phys. Rev. Appl.* **11**, 044092 (2019).
- [12] N. Lacroix, C. Hellings, C. K. Andersen, A. Di Paolo, A. Remm, S. Lazar, S. Krinner, G. J. Norris, M. Gabureac, J. Heinsoo, A. Blais, C. Eichler, and A. Wallraff, Improving the Performance of Deep Quantum Optimization Algorithms with Continuous Gate Sets, *PRX Quantum* **1**, 110304 (2020).
- [13] A. D. Hill, M. J. Hodson, N. Didier, and M. J. Reagor, Realization of arbitrary doubly-controlled quantum phase gates, *ArXiv:2108.01652* (2021).
- [14] E. Farhi, J. Goldstone, and S. Gutmann, A quantum approximate optimization algorithm, *ArXiv:1411.4028* (2014).
- [15] M. P. Harrigan, K. J. Sung, M. Neeley, K. J. Satzinger, F. Arute, K. Arya, J. Atalaya, J. C. Bardin, R. Barends, and S. Boixo, *et al.*, Quantum approximate optimization of non-planar graph problems on a planar superconducting processor, *Nat. Phys.* **17**, 332 (2021).
- [16] A. Barenco, C. H. Bennett, R. Cleve, D. P. DiVincenzo, N. Margolus, P. Shor, T. Sleator, J. A. Smolin, and H. Woerner, Elementary gates for quantum computation, *Phys. Rev. A* **52**, 3457 (1995).
- [17] J. J. Vartiainen, M. Möttönen, and M. M. Salomaa, Efficient Decomposition of Quantum Gates, *Phys. Rev. Lett.* **92**, 177902 (2004).
- [18] V. V. Shende and I. L. Markov, On the CNOT-cost of Toffoli gates, *Quantum Inf. Comput.* **9**, 461 (2009).
- [19] Y. Shi, Both Toffoli and controlled-NOT need little help to do universal quantum computation, *ArXiv:quant-ph/0205115* (2002).
- [20] B. Foxen, *et al.*, Demonstrating a Continuous Set of Two-Qubit Gates for Near-Term Quantum Algorithms, *Phys. Rev. Lett.* **125**, 120504 (2020).
- [21] D. M. Abrams, N. Didier, B. R. Johnson, M. P. d. Silva, and C. A. Ryan, Implementation of XY entangling gates with a single calibrated pulse, *Nat. Electron.* **3**, 744 (2020).
- [22] K. Mølmer and A. Sørensen, Multiparticle Entanglement of Hot Trapped Ions, *Phys. Rev. Lett.* **82**, 1835 (1999).
- [23] D. Kielpinski, C. Monroe, and D. J. Wineland, Architecture for a large-scale ion-trap quantum computer, *Nature* **417**, 709 (2002).
- [24] F. Kranzl, M. K. Joshi, C. Maier, T. Brydges, J. Franke, R. Blatt, and C. F. Roos, Controlling long ion strings for quantum simulation and precision measurements, *Phys. Rev. A* **105**, 052426 (2022).
- [25] A. S. Sørensen and K. Mølmer, Measurement Induced Entanglement and Quantum Computation with Atoms in Optical Cavities, *Phys. Rev. Lett.* **91**, 097905 (2003).
- [26] J. Ramette, J. Sinclair, Z. Vendeiro, A. Rudelis, M. Cetina, and V. Vuletić, Any-To-Any Connected Cavity-Mediated Architecture for Quantum Computing with Trapped Ions or Rydberg Arrays, *PRX Quantum* **3**, 010344 (2022).
- [27] M. Mariantoni, H. Wang, T. Yamamoto, M. Neeley, R. C. Bialczak, Y. Chen, M. Lenander, E. Lucero, A. D. O'Connell, D. Sank, M. Weides, J. Wenner, Y. Yin, J. Zhao, A. N. Korotkov, A. N. Cleland, and J. M. Martinis, Implementing the quantum von Neumann architecture with superconducting circuits, *Science* **334**, 61 (2011).
- [28] A. Fedorov, L. Steffen, M. Baur, M. P. da Silva, and A. Wallraff, Implementation of a Toffoli gate with superconducting circuits, *Nature* **481**, 170 (2012).
- [29] A. S. Nikolaeva, E. O. Kiktenko, and A. K. Fedorov, Decomposing the generalized Toffoli gate with qutrits, *Phys. Rev. A* **105**, 032621 (2022).
- [30] J. Chu, *et al.*, Scalable algorithm simplification using quantum AND logic, *Nat. Phys.* **19**, 126 (2023).
- [31] Y. Kim, A. Morvan, L. B. Nguyen, R. K. Naik, C. Jünger, L. Chen, J. M. Kreikebaum, D. I. Santiago, and I. Siddiqi, High-fidelity three-qubit i Toffoli gate for fixed-frequency superconducting qubits, *Nat. Phys.* **18**, 783 (2022).
- [32] A. J. Baker, G. B. Huber, N. J. Glaser, F. Roy, I. Tsitsilin, S. Filipp, and M. J. Hartmann, Single shot i -Toffoli gate in dispersively coupled superconducting qubits, *Appl. Phys. Lett.* **120**, 054002 (2022).
- [33] X. Gu, J. Fernández-Pendás, P. Vikstål, T. Abad, C. Warren, A. Bengtsson, G. Tancredi, V. Shumeiko, J. Bylander, G. Johansson, and A. F. Kockum, Fast Multiqubit Gates through Simultaneous Two-Qubit Gates, *PRX Quantum* **2**, 040348 (2021).
- [34] M. Nägele, C. Schweizer, F. Roy, and S. Filipp, Effective nonlocal parity-dependent couplings in qubit chains, *Phys. Rev. Res.* **4**, 033166 (2022).

- [35] K. Zhang, H. Li, P. Zhang, J. Yuan, J. Chen, W. Ren, Z. Wang, C. Song, D.-W. Wang, H. Wang, S. Zhu, G. S. Agarwal, and M. O. Scully, Synthesizing Five-Body Interaction in a Superconducting Quantum Circuit, *Phys. Rev. Lett.* **128**, 190502 (2022).
- [36] A. Mezzacapo, L. Lamata, S. Filipp, and E. Solano, Many-Body Interactions with Tunable-Coupling Transmon Qubits, *Phys. Rev. Lett.* **113**, 050501 (2014).
- [37] H. Paik, A. Mezzacapo, M. Sandberg, D. T. McClure, B. Abdo, A. D. Córcoles, O. Dial, D. F. Bogorin, B. L. T. Plourde, M. Steffen, A. W. Cross, J. M. Gambetta, and J. M. Chow, Experimental Demonstration of a Resonator-Induced Phase Gate in a Multiqubit Circuit-QED System, *Phys. Rev. Lett.* **117**, 250502 (2016).
- [38] C. Song, K. Xu, W. Liu, C.-P. Yang, S.-B. Zheng, H. Deng, Q. Xie, K. Huang, Q. Guo, and L. Zhang, *et al.*, 10-Qubit Entanglement and Parallel Logic Operations with a Superconducting Circuit, *Phys. Rev. Lett.* **119**, 180511 (2017).
- [39] M. Lu, J.-L. Ville, J. Cohen, A. Petrescu, S. Schreppler, L. Chen, C. Jünger, C. Pelletti, A. Marchenkov, A. Banerjee, W. P. Livingston, J. M. Kreikebaum, D. I. Santiago, A. Blais, and I. Siddiqi, Multipartite Entanglement in Rabi-Driven Superconducting Qubits, *PRX Quantum* **3**, 040322 (2022).
- [40] C. Song, K. Xu, H. Li, Y.-R. Zhang, X. Zhang, W. Liu, Q. Guo, Z. Wang, W. Ren, and J. Hao, *et al.*, Generation of multicomponent atomic Schrödinger cat states of up to 20 qubits, *Science* **365**, 574 (2019).
- [41] T. Menke, W. P. Banner, T. R. Bergamaschi, A. Di Paolo, A. Vepsäläinen, S. J. Weber, R. Winik, A. Melville, B. M. Niedzielski, D. Rosenberg, K. Serniak, M. E. Schwartz, J. L. Yoder, A. Aspuru-Guzik, S. Gustavsson, J. A. Grover, C. F. Hirjibehedin, A. J. Kerman, and W. D. Oliver, Demonstration of Tunable Three-Body Interactions between Superconducting Qubits, *Phys. Rev. Lett.* **129**, 220501 (2022).
- [42] F. Yan, P. Krantz, Y. Sung, M. Kjaergaard, D. Campbell, J. I. J. Wang, T. P. Orlando, S. Gustavsson, and W. D. Oliver, A Tunable Coupling Scheme for Implementing High-Fidelity Two-Qubit Gates, *Phys. Rev. Appl.* **10**, 054062 (2018).
- [43] M. C. Collodo, J. Herrmann, N. Lacroix, C. K. Andersen, A. Remm, S. Lazar, J.-C. Besse, T. Walter, A. Wallraff, and C. Eichler, *et al.*, Implementation of Conditional Phase Gates Based on Tunable ZZ Interactions, *Phys. Rev. Lett.* **125**, 240502 (2020).
- [44] Y. Xu, J. Chu, J. Yuan, J. Qiu, Y. Zhou, L. Zhang, X. Tan, Y. Yu, S. Liu, J. Li, F. Yan, and D. Yu, High-Fidelity, High-Scalability Two-Qubit Gate Scheme for Superconducting Qubits, *Phys. Rev. Lett.* **125**, 240503 (2020).
- [45] J. Chu and F. Yan, Coupler-Assisted Controlled-Phase Gate with Enhanced Adiabaticity, *Phys. Rev. Appl.* **16**, 054020 (2021).
- [46] J. Stehlik, D. Zajac, D. Underwood, T. Phung, J. Blair, S. Carnevale, D. Klaus, G. Keefe, A. Carniol, M. Kumph, M. Steffen, and O. Dial, Tunable Coupling Architecture for Fixed-Frequency Transmon Superconducting Qubits, *Phys. Rev. Lett.* **127**, 080505 (2021).
- [47] J. Koch, T. M. Yu, J. Gambetta, A. A. Houck, D. I. Schuster, J. Majer, A. Blais, M. H. Devoret, S. M. Girvin, and R. J. Schoelkopf, *et al.*, Charge-insensitive qubit design derived from the Cooper pair box, *Phys. Rev. A* **76**, 042319 (2007).
- [48] D. C. McKay, S. Filipp, A. Mezzacapo, E. Magesan, J. M. Chow, and J. M. Gambetta, A Universal Gate for Fixed-Frequency Qubits via a Tunable Bus, *Phys. Rev. Appl.* **6**, 064007 (2016).
- [49] Y. Sung, L. Ding, J. Braumüller, A. Vepsäläinen, B. Kannan, M. Kjaergaard, A. Greene, G. O. Samach, C. McNally, D. Kim, A. Melville, B. M. Niedzielski, M. E. Schwartz, J. L. Yoder, T. P. Orlando, S. Gustavsson, and W. D. Oliver, Realization of High-Fidelity CZ and ZZ-Free iSWAP Gates with a Tunable Coupler, *Phys. Rev. X* **11**, 021058 (2021).
- [50] Y. Chen, *et al.*, Qubit Architecture with High Coherence and Fast Tunable Coupling, *Phys. Rev. Lett.* **113**, 220502 (2014).
- [51] E. A. Sete, N. Didier, A. Q. Chen, S. Kulshreshtha, R. Manenti, and S. Poletto, Parametric-Resonance Entangling Gates with a Tunable Coupler, *Phys. Rev. Appl.* **16**, 024050 (2021).
- [52] D. C. McKay, C. J. Wood, S. Sheldon, J. M. Chow, and J. M. Gambetta, Efficient z gates for quantum computing, *Phys. Rev. A* **96**, 022330 (2017).
- [53] S. Meiboom and D. Gill, Modified spin-echo method for measuring nuclear relaxation times, *Rev. Sci. Instrum.* **29**, 688 (1958).
- [54] U. Haeberlen and J. S. Waugh, Coherent averaging effects in magnetic resonance, *Phys. Rev.* **175**, 453 (1968).
- [55] A. Brinkmann, Introduction to average Hamiltonian theory. I. Basics, *Concepts Magn. Reson. A* **45**, e21414 (2016).
- [56] E. L. Hahn, Spin echoes, *Phys. Rev.* **80**, 580 (1950).
- [57] H. Y. Carr and E. M. Purcell, Effects of diffusion on free precession in nuclear magnetic resonance experiments, *Phys. Rev.* **94**, 630 (1954).
- [58] F. Motzoi, J. M. Gambetta, P. Rebentrost, and F. K. Wilhelm, Simple Pulses for Elimination of Leakage in Weakly Nonlinear Qubits, *Phys. Rev. Lett.* **103**, 110501 (2009).
- [59] M. J. Peterer, S. J. Bader, X. Jin, F. Yan, A. Kamal, T. J. Gudmundsen, P. J. Leek, T. P. Orlando, W. D. Oliver, and S. Gustavsson, *et al.*, Coherence and Decay of Higher Energy Levels of a Superconducting Transmon Qubit, *Phys. Rev. Lett.* **114**, 010501 (2015).
- [60] J. J. Burnett, A. Bengtsson, M. Scigliuzzo, D. Niepce, M. Kudra, P. Delsing, and J. Bylander, Decoherence benchmarking of superconducting qubits, *npj Quantum Inf.* **5**, 54 (2019).
- [61] M. A. Rol, F. Battistel, F. K. Malinowski, C. C. Bultink, B. M. Tarasinski, R. Vollmer, N. Haider, N. Muthusubramanian, A. Bruno, B. M. Terhal, and L. DiCarlo, Fast, High-Fidelity Conditional-Phase Gate Exploiting Leakage Interference in Weakly Anharmonic Superconducting Qubits, *Phys. Rev. Lett.* **123**, 120502 (2019).
- [62] A. P. M. Place, *et al.*, New material platform for superconducting transmon qubits with coherence times exceeding 0.3 milliseconds, *Nat. Commun.* **12**, 1779 (2021).
- [63] C. Wang, X. Li, H. Xu, Z. Li, J. Wang, Z. Yang, Z. Mi, X. Liang, T. Su, and C. Yang, *et al.*, Towards practical quantum computers: Transmon qubit with a lifetime approaching 0.5 milliseconds, *npj Quantum Inf.* **8**, 3 (2022).
- [64] B. G. Christensen, C. D. Wilen, A. Opremcak, J. Nelson, F. Schlenker, C. H. Zimonick, L. Faoro, L. B. Ioffe, Y. J.

- Rosen, J. L. DuBois, B. L. T. Plourde, and R. McDermott, Anomalous charge noise in superconducting qubits, *Phys. Rev. B* **100**, 140503 (2019).
- [65] C. W. Warren, J. Fernández-Pendás, S. Ahmed, T. Abad, A. Bengtsson, J. Biznárová, K. Debnath, X. Gu, C. Križan, A. Osman, A. F. Roudsari, P. Delsing, G. Johansson, A. F. Kockum, G. Tancredi, and J. Bylander, Extensive characterization of a family of efficient three-qubit gates at the coherence limit, *ArXiv:2207.02938* (2022).
- [66] S. N. Shevchenko, S. Ashhab, and F. Nori, Landau-zener-stückelberg interferometry, *Phys. Rep.* **492**, 1 (2010).
- [67] J. Roland and N. J. Cerf, Quantum search by local adiabatic evolution, *Phys. Rev. A* **65**, 042308 (2002).
- [68] N. Wittler, F. Roy, K. Pack, M. Werninghaus, A. S. Roy, D. J. Egger, S. Filipp, F. K. Wilhelm, and S. Machnes, Integrated Tool Set for Control, Calibration, and Characterization of Quantum Devices Applied to Superconducting Qubits, *Phys. Rev. Appl.* **15**, 034080 (2021).
- [69] Zurich Instruments AG, HDAWG user manual. See https://docs.zhinst.com/pdf/ziHDAWG_UserManual.pdf.
- [70] V. Negîrneac, H. Ali, N. Muthusubramanian, F. Battistel, R. Sagastizabal, M. S. Moreira, J. F. Marques, W. J. Vlothuizen, M. Beekman, C. Zachariadis, N. Haider, A. Bruno, and L. DiCarlo, High-Fidelity Controlled-z Gate with Maximal Intermediate Leakage Operating at the Speed Limit in a Superconducting Quantum Processor, *Phys. Rev. Lett.* **126**, 220502 (2021).